nature nanotechnology

ARTICLES

https://doi.org/10.1038/s41565-021-00915-2

Check for updates

Foldamer-based ultrapermeable and highly selective artificial water channels that exclude protons

Arundhati Roy[1,2,8], Jie Shen[1,8], Himanshu Joshi[3], Woochul Song[4], Yu-Ming Tu[4], Ratul Chowdhury[5], Ruijuan Ye[1], Ning Li[2], Changliang Ren[2], Manish Kumar[6], Aleksei Aksimentiev[3] and Huaqiang Zeng[1,7] ✉

The outstanding capacity of aquaporins (AQPs) for mediating highly selective superfast water transport[1–7] has inspired recent development of supramolecular monovalent ion-excluding artificial water channels (AWCs). AWC-based bioinspired membranes are proposed for desalination, water purification and other separation applications[8–18]. While some recent progress has been made in synthesizing AWCs that approach the water permeability and ion selectivity of AQPs, a hallmark feature of AQPs—high water transport while excluding protons—has not been reproduced. We report a class of biomimetic, helically folded pore-forming polymeric foldamers that can serve as long-sought-after highly selective ultrafast water-conducting channels with performance exceeding those of AQPs (1.1×10^{10} water molecules per second for AQP1), with high water-over-monovalent-ion transport selectivity (~10^8 water molecules over Cl^- ion) conferred by the modularly tunable hydrophobicity of the interior pore surface. The best-performing AWC reported here delivers water transport at an exceptionally high rate, namely, 2.5 times that of AQP1, while concurrently rejecting salts (NaCl and KCl) and even protons.

Drawing on nature for inspiration, biomimicry has provided rich and effective technological solutions to a range of complex problems[19]. One challenging line of inquiry in biomimicry is the extent to which man-made materials can mimic nature or even go beyond the boundaries seen in nature at the macro- and nanoscales. At the molecular level, biological channels play indispensable roles in myriad cellular processes via precisely controlled directional flows of cognate species (including water[1–7], potassium[20], sodium[21], calcium[22], chloride[23] and protons[24]). These precisely controlled flows occur through narrow—often water-filled—membrane-spanning pores. Nevertheless, the two highly integrated quintessential features collectively seen in many natural membrane channels—high selectivity that is seamlessly integrated with high permeation rate—are exceedingly difficult to replicate in artificially developed membrane materials[12], particularly artificial channels and carriers. In fact, despite numerous advances made over the past four decades[15–18,25–44], no artificial channels or membranes have reached the performance in transmembrane transport of ions, protons or water molecules seen in biological channels such as the potassium channel (KcsA) and aquaporins (AQPs). The unique ability of AQPs to exclude protons while transporting water decouples water transport from the maintenance of transmembrane proton gradients[45], which has not been previously reproduced in artificial channels or engineered biological channels. Through a minimalist biomimetic approach, we have succeeded in outperforming AQP1 (refs. [1–7]) in water transport rate while concurrently retaining high rejection of both salts (NaCl and KCl) and protons.

The outstanding water and ion transport performance of AQP1 (~1.1×10^{10} water molecules per second (ref. [7]) while excluding all ions), estimated at >10^9 water molecules over monovalent ions[46], has inspired the development of AQP-based biomimetic membranes for industrial and municipal desalting and water purification applications[8–18]. Protein-based membranes, however, are expected to have a high production cost and face perceived challenges with scaling up and stability for industrial uses[11]. These challenges may limit their widespread applications in novel membrane technologies for water purification and other applications including blue energy production, organic solvent nanofiltration and organic solvent reverse osmosis[18]. Mimicking the functions of AQPs for enabling a wider range of molecular separation applications, bioinspired supramolecular artificial water channels (AWCs) have emerged as promising materials[25–34]. Yet, concurrently attaining high single-channel water permeability and high transport selectivity has proven to be challenging. Indeed, among all hitherto reported AWCs with high selectivity[25–33], self-assembled AWCs that reject salts have only been recently reported, and they transport water at a rate of 3.0×10^9 water molecules per second (refs. [31,33]), which is ~27% that of AQP1. Carbon nanotube porins (CNTPs) with an internal pore diameter of 4.7 Å exhibit a water conduction rate 2.1 times that of AQP1 (ref. [34]). However, CNTPs also conduct Na^+, K^+ and other protons[34,41].

Molecular design principles and considerations for AWCs

In this work, we aim to mimic the water transport function of AQPs using a set of selectivity principles and structural motifs not found

[1]Department of Chemistry, College of Science, Hainan University, Haikou, Hainan, China. [2]NanoBio Lab, 31 Biopolis Way, The Nanos, Singapore. [3]Department of Physics and Beckman Institute for Advanced Science and Technology, University of Illinois at Urbana–Champaign, Urbana, IL, USA. [4]Department of Chemical Engineering, The University of Texas at Austin, Austin, TX, USA. [5]Department of Chemical Engineering, The Pennsylvania State University, University Park, PA, USA. [6]Department of Civil, Architectural and Environmental Engineering, The University of Texas at Austin, Austin, TX, USA. [7]Institute of Advanced Synthesis, Northwestern Polytechnical University, Xi'an, Shaanxi, China. [8]These authors contributed equally: Arundhati Roy, Jie Shen. ✉e-mail: 2733910004@qq.com

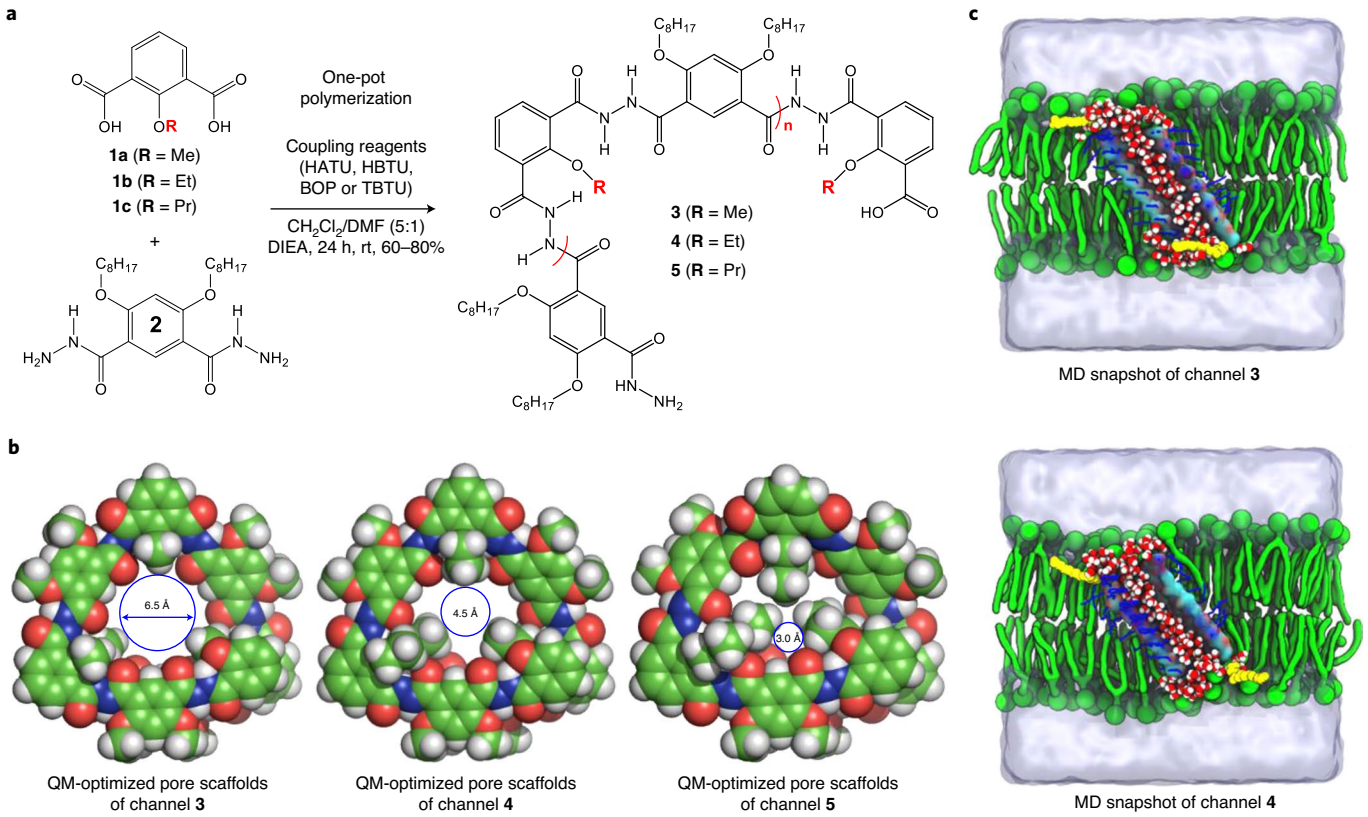

Fig. 1 | Molecular design and synthesis of foldamer-derived polymer-based synthetic water channels. a, Chemical structures of AWCs **3**–**5**, which have inwardly facing methyl (**3**), ethyl (**4**) or isopropyl (**5**) aliphatic groups for tuning the inner-pore size and hydrophobicity. **b**, QM-optimized backbone scaffolds of **3**–**5**, illustrating excellent structural correspondence to the crystallographic structures of methyl- and ethyl-containing trimeric repeating units (see **6a** and **6b** in Supplementary Fig. 1b for details). **c**, Cross-sections of MD snapshots of water-filled LA-terminated channels **3** and **4**, each containing 26 units of **1** and 25 units of **2** and having a height of 2.9 nm, in a POPC membrane. The system is solvated in 1 M NaCl, with the volume occupied by the electrolyte solution represented as a semi-transparent surface. HATU, 1-[Bis(dimethylamino)methylene]-1H-1,2,3-triazolo[4,5-b]pyridinium 3-oxide hexafluorophosphate; HBTU, hexafluorophosphate benzotriazole tetramethyl uronium; TBTU, tetramethyl-O-(benzotriazol-1-yl)uronium tetrafluoroborate; BOP, benzotriazol-1-yloxytris(dimethylamino)phosphonium hexafluorophosphate; DIEA, diisopropylethylamine; POPC, 1-palmitoyl-2-oleoyl-*sn*-glycero-3-phosphatidyl choline; rt, room temperature.

in AQPs. We speculated that a large hollow tubular cavity, possessing a pore diameter much larger than a water molecule (2.5 Å) but still smaller than a Na^+ ion with its first hydration shell (~9 Å; Supplementary Fig. 1a), might be needed to compete with AQPs. More precisely, we wanted to investigate if water transport that does not strictly adhere to the single-file water arrangement in AQP1 and other channels[32–34] might be able to enable water transport rates higher than AQP1.

We attain high salt rejection by these large pores by decorating the interior pore surface with functional groups, which are 'incompetent' in replacing ion-coordinated water molecules, thereby increasing the barrier to ion entry and passage through the channels[40]. The overall strategy implemented here further involved the use of aliphatic chains to render the cavity hydrophobic. Differing from π-electron-rich hydrophobicity in CNTs that could interact with cations[47], such 'aliphatic hydrophobicity' conferred by the essentially non-polar C–H bonds provides a slightly positive electrostatic surface[40] that excludes cations. Although the aliphatic hydrophobic surface has been shown to favourably interact with anions[48,49], a sufficiently small hydrophobic cavity (for example, 4.3 Å in **4**) may block anion transport. Moreover, we focused on designs where one-dimensional H-bonded water chains cannot be continuously formed inside the pores. This was achieved by obstructing continuous proton transfer to adjacent water molecules, thereby blocking proton transport. In doing so, fluctuation of hydrophobic groups disrupts the water wire, distinct from that in the asparagine–proline–alanine motif, centrally located in AQPs (ref. [50]). This work also addresses the question of whether continuously formed H-bonded water chains (seen in CNTPs (ref. [34]) and other channels[32,33]) are essential for rapid water transport.

Molecular design and structural features of AWCs 3–5

We recently reported polymeric channel **3** (Fig. 1a) derived from an H-bond-rigidified foldamer-based hydrazide backbone[40]. Arising from hydrophobic methyl groups, the well-separated interior O atoms (cavity of ~6.5 Å) cannot form a convergent cation-binding pocket (Fig. 1b), but it allows anion transport. Considering these design principles, the interior methyl groups (Me) in **3** were replaced by ethyl (Et) or propyl (Pr) groups to afford two new classes of polymer channels **4** and **5**, having smaller hydrophobic cavities to minimize anion-specific interactions.

Quantum mechanics (QM) calculations of pore scaffolds at the ωB97X/6-31 + G(d) level were adopted to understand the structural features of **3**–**5**. The central fragments of the QM-computed pores of **3** and **4** (Fig. 1b) are nearly identical to the crystal structures of trimer molecules **6a** and **6b**, respectively, indicating high reliability of the computed pore sizes of ≥6.5 Å for **3**, ≥4.3 Å for **4**, and three segregated pores of ~2.7 Å for **5**. Based on these QM-derived

structures, we built 2.9-nm-long channel structures **3**–**5**, each having 26 units of **1** and 25 units of **2**. All-atom molecular dynamics (MD) simulation[2,4] was conducted by embedding channels in a POPC lipid membrane surrounded by 1 M NaCl to provide further structural insights. As expected, both **3** and **4** enclose a water-filled sizable cavity of >4 Å (Fig. 1c and Supplementary Fig. 1c), whereas the cavity of **5** is mostly blocked by the Pr groups (Supplementary Fig. 1c).

High water permeability of AWCs 3–5

Following a recently reported one-pot polymerization protocol[40], 12 AWCs (**3**–**5**) were readily made from repeating units **1** and **2** and four coupling reagents (HATU, HBTU, BOP and TBTU; Fig. 1a, Supplementary Fig. 2 and Supplementary Tables 1–3), with GPC-derived molecular weights (M_n) of 11.6–27.3 KDa and nanotube lengths of 2.1–5.1 nm.

Single-channel water permeability (P_{sc} in $cm^3\,s^{-1}$) was investigated by a stopped-flow method[25–34], using 0.3 M sucrose as the draw solution. To facilitate quick identification of effective AWCs, 100% channel membrane insertion efficiency was assumed for all the channels, which turns out to be a valid one as the actual channel insertion efficiencies were found to be nearly identical among **3**–**5** under identical conditions (see discussion later). By varying the lipid-to-channel molar ratios (mLCR) from 1,500:1 to 9,000:1, 3.0-nm-long channel **3** synthesized using HATU was found to elicit the maximum permeability at mLCR of 6,000:1 (Supplementary Fig. 3 and Supplementary Table 4). Keeping the mLCR fixed at 6,000:1, P_{sc} values appear to plateau at a channel height of 3.0 nm ($7.75\pm0.76\times10^{-14}\,cm^3\,s^{-1}$) among series **3**, 3.1 nm ($8.97\pm0.76\times10^{-14}\,cm^3\,s^{-1}$) among series **4** and 2.1 nm ($14.72\pm0.97\times10^{-14}\,cm^3\,s^{-1}$) among series **5** (Supplementary Table 5). These values translate into water transport rates of ~10^9 water molecules per second.

Ultrapermeability of 4-LA

We surmised that **3** and **4** likely could transport water molecules much faster than ~10^9 water molecules per second because their pore sizes are much larger than a water molecule. Channels **3** and **4** lack hydrophilic end groups for aligning channels to span lipid bilayers seen in other water channels, leading us to hypothesize that many channel orientations not conducive for water transport may exist. To examine this, carboxylic acid-based 'lipid anchors' (LAs; Fig. 2a) were attached at both termini of the most active channels among series **3**, **4** and **5** to produce **3-LA**, **4-LA** and **5-LA**, respectively, and evaluate their water transport activity.

Compared with **3** (which is free of LAs), the water conduction of **3-LA** was greatly improved (Fig. 2b), and its P_{sc} value averaged over three runs was determined to be $36.58\pm1.97\times10^{-14}\,cm^3\,s^{-1}$ at an mLCR of 6,000:1 (Fig. 2c). Similarly, P_{sc} values of **4-LA** and **5-LA** were increased to $60.14\pm0.17\times10^{-14}\,cm^3\,s^{-1}$ and $18.12\pm1.76\times10^{-14}\,cm^3\,s^{-1}$, respectively. After corrections using channel insertion efficiencies of 66%, 75% and 75% for **3-LA**, **4-LA** and **5-LA**, respectively (Supplementary Fig. 4 and Supplementary Table 6), their respective water conduction rates were determined to be $1.6\pm0.060\times10^{10}$, $2.7\pm0.005\times10^{10}$ and $0.8\pm0.050\times10^{10}$ water molecules per second. In particular, the **4-LA**-mediated ultrafast water conduction of 2.7×10^{10} water molecules per second represents a large improvement of 145% over that of AQP1 (1.1×10^{10} water molecules per second (ref. [7])) and is even higher than that of CNTPs (2.3×10^{10} water molecules per second (ref. [34])) at pH 7.

The water transport activation energy values (E_a) for 1,2-dioleoyl-*sn*-glycero-3-phosphocholine (DOPC) membrane alone, **3-LA**, **4-LA** and **5-LA** were determined to be 12.3 ± 1.3, 8.7 ± 1.2, 8.3 ± 0.9 and 11.5 ± 1.2 kcal mol^{-1}, respectively (Supplementary Fig. 5). Consistent with recent observations by us[32,33] and others[4,33], E_a value for the more permeable **4-LA**—while lower than a pure lipid membrane—turns out to be larger than that of less permeable AQP1 (~5 kcal mol^{-1}) (ref. [5]). This suggests that the low E_a seen in AQP channels[7,51] may not be a requirement for all highly permeable channels, particularly when the transport is not strictly mediated by a single water wire. Horner et al. have recently shown that reduced friction, which at the molecular level corresponds to a lower number of H-bonds between the water molecules and the channel-lining residues, could increase the water permeability 100-fold (ref. [51]). We have also shown that three factors (namely, pore volume, friction and deviation from optimum H-bonded water chain structure) collectively yet decisively contribute to a 15-fold difference in the single-channel permeability[33]. Therefore, although **3-LA** and **4-LA** have similar E_a values (8.7 ± 1.2 and 8.3 ± 0.9 kcal mol^{-1}), which is larger than ~5 kcal mol^{-1} for AQPs, we speculate that it is the hydrophobic alkyl groups that generate pores with lower friction to facilitate higher water transport rates than AQPs. In addition, ethyl-containing **4-LA** may have more hydrophobic pores that experience smaller resistance, resulting in faster transport rate than **3-LA**. Further, given that E_a is a measure of the enthalpic energy barrier for transport in narrow channels but entropic barriers could also be important, we suspect that entropy may be part of the answer to why **3-LA** and **4-LA** exhibit faster water transport than AQPs while having higher E_a values.

High rejection of salts and protons by 4-LA

Another indispensable criterion of being an ideal AWC is the ability to reject salts (KCl and NaCl) and, ideally, protons. At an mLCR of 6,000:1, the measured osmotic permeability coefficient (P_f) values for **4-LA** were 117.5 ± 4.5, 121.5 ± 3.8 and 124.7 ± 0.3 cm s^{-1} for sucrose, NaCl and KCl, respectively. The corresponding reflection coefficients, defined as the ratio of P_f values, are 1.03 ± 0.010 for P_f (NaCl)/P_f (sucrose) and 1.06 ± 0.006 for P_f (KCl)/P_f (sucrose), suggesting that **4-LA** achieves high rejection of NaCl and KCl (refs. [28,32,33]). These approximate values indicating salt rejection can be corroborated by the low reflection coefficients of 0.53 ± 0.020 and 0.07 ± 0.001 for gramicidin A (gA) cation channel, which is highly permeable to both Na^+ and K^+ ions, respectively.

High rejection of Na^+ and K^+ was validated further by using assays employing large unilamellar vesicles (LUVs) of about 120 nm in diameter, with entrapped pH-sensitive HPTS dye (Fig. 2d). Unsurprisingly, both **4** and **4-LA** at 1 μM are completely inactive towards both K^+ and Na^+ ions, whereas dimeric gA—at a channel concentration 20 times smaller (0.1 μM)—transports both Na^+ (114%) and K^+ (118%) at higher rates. The presence of **4-LA** in the membrane can be established by the measured membrane insertion efficiency of ≥75% under identical conditions (Supplementary Fig. 7). Additional testing similarly reveals high cation rejections by **3**, **3-LA**, **5** and **5-LA** (Supplementary Fig. 8a), demonstrating that a pore as large as 6.5 Å in **3** can effectively prevent both Na^+ and K^+ ions from entering it, along with the smaller, mostly hydrophobic pores in **4** and **5**.

High rejection of Cl^- and protons can also be confirmed using the LUV scheme shown in Fig. 2e. Specifically, compared with a self-assembled chloride channel $(\mathbf{F8})_6$ (ref. [52]) that induces a high chloride transport activity of 138%, and to the proton carrier FCCP (carbonyl cyanide 4-(trifluoromethoxy)phenylhydrazone) that induces a high proton transport activity of 112%, both the anion and proton transport rates of **3-LA**, **4**, **4-LA** (Fig. 2e), **5** and **5-LA** (Supplementary Fig. 8b) were non-detectable. A large difference in Cl^- transport between **3** and **3-LA** can be ascribed to the fact that the LA in **3-LA** contains a carboxylic acid group, ionizing to become a negatively charged carboxylate anion at pH 7. These negative charges at the channel's two ends may reduce the chance of an anion entering the transmembrane pore, attenuating the otherwise high anion transport activity of **3** (ref. [40]). Additionally, a conservative estimate indicates the **4-LA**-induced proton transport rate to be <0.01 protons per second (Supplementary Fig. 9 and corresponding

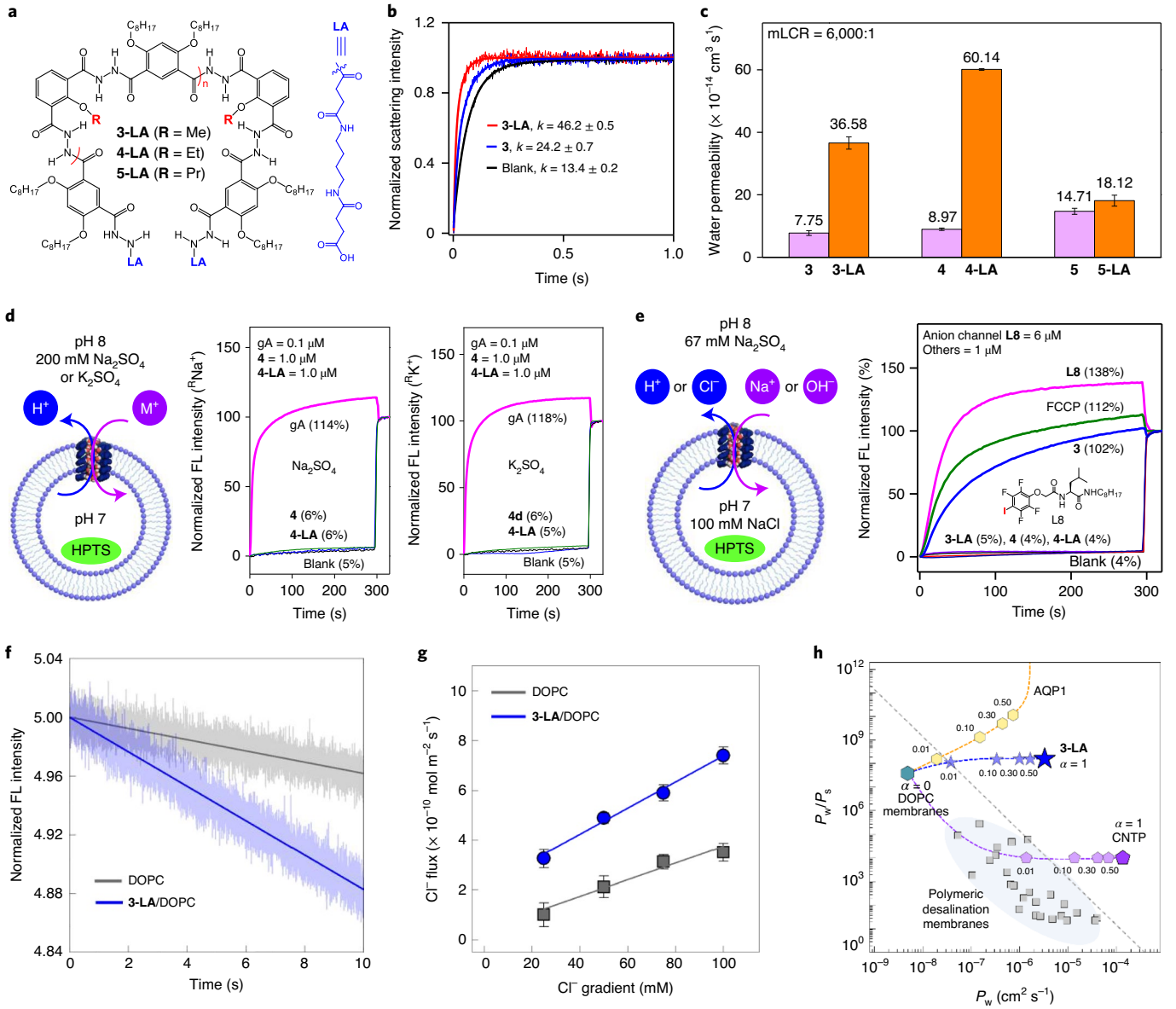

Fig. 2 | Selective water permeation through foldamer-based polymeric AWCs. a, Chemical structures of **LA**-modified AWCs. **b**, Representative stopped-flow light scattering traces of **3**- and **3-LA**-reconstituted DOPC vesicles under the inwardly directed osmotic gradients. **c**, Single-channel permeability before and after **LA** modification. **d**,**e**, Schematic of HPTS-based fluorescence assays, demonstrating high rejection of cations (Na^+ or K^+) (**d**) and anion (Cl^-) and proton (**e**) through the channels. ${}^{R}M^{+} = (I_{M+} - I_0)/(I_{Triton} - I_0)$. **f**, Stopped-flow fluorescence traces of **3-LA**-reconstituted DOPC vesicles, encapsulating lucigenin dyes for sensing Cl^- permeation that is driven by inwardly directed Cl^- concentration gradients (20 mM). FL, fluorescence. **g**, Plots of Cl^- permeation flux as a function of Cl^- concentration gradients for both DOPC and **3-LA**-reconstituted DOPC membranes. **h**, Comparison of water-to-salt permselectivity of **3-LA** to the values of several representative water channels and current polymeric desalination membranes. Intrinsic water-to-salt selectivity (P_w/P_s) versus water permeability (P_w; $cm^2\,s^{-1}$) plot. P_w/P_s versus P_w values for **3-LA**-reconstituted biomimetic membranes in a DOPC matrix, which were compared with other representative water channels, AQP1 and CNTPs with a pore diameter of ~0.47 nm (refs. [13,34]). The α values in the plot indicate the fractional area of the biomimetic membranes occupied by water channels (for example, $\alpha = 0.5$ represents the membranes in which half the surface area is composed of channels). The dashed line is the permeability–selectivity upper bound of currently available polymer desalination membranes[10,12]. Data in **c**,**f** and **g** are the average of three independent measurements with error bars representing the standard deviations. HPTS, 8-hydroxypyrene-1,3,6-trisulfonic acid.

discussions) at pH 7. This value is in great agreement with the quantitative proton permeation rate of <0.1 protons per second measured using stopped-flow fluorescence spectroscopy (Supplementary Figs. 10–12).

High rejection of Cl^- also can be established by using a chloride-sensitive SPQ dye (6-methoxy-N-(3-sulfopropyl)quinolinium, Supplementary Fig. 8c). Except for **3**, the channels **3-LA**, **4**, **4-LA**, **5** and **5-LA** quenched the SPQ dye undifferentiated from the background, whereas $(F8)_6$ displayed 45% fluorescence quenching. Thus, results of these LUV-based assays provide evidence of high rejection of both salts and protons by ultrapermeable **4-LA** and by superpermeable **3-LA**, **4**, **5** and **5-LA**.

To evaluate the molecular separation property of the channels for desalination applications, monovalent ion permeability

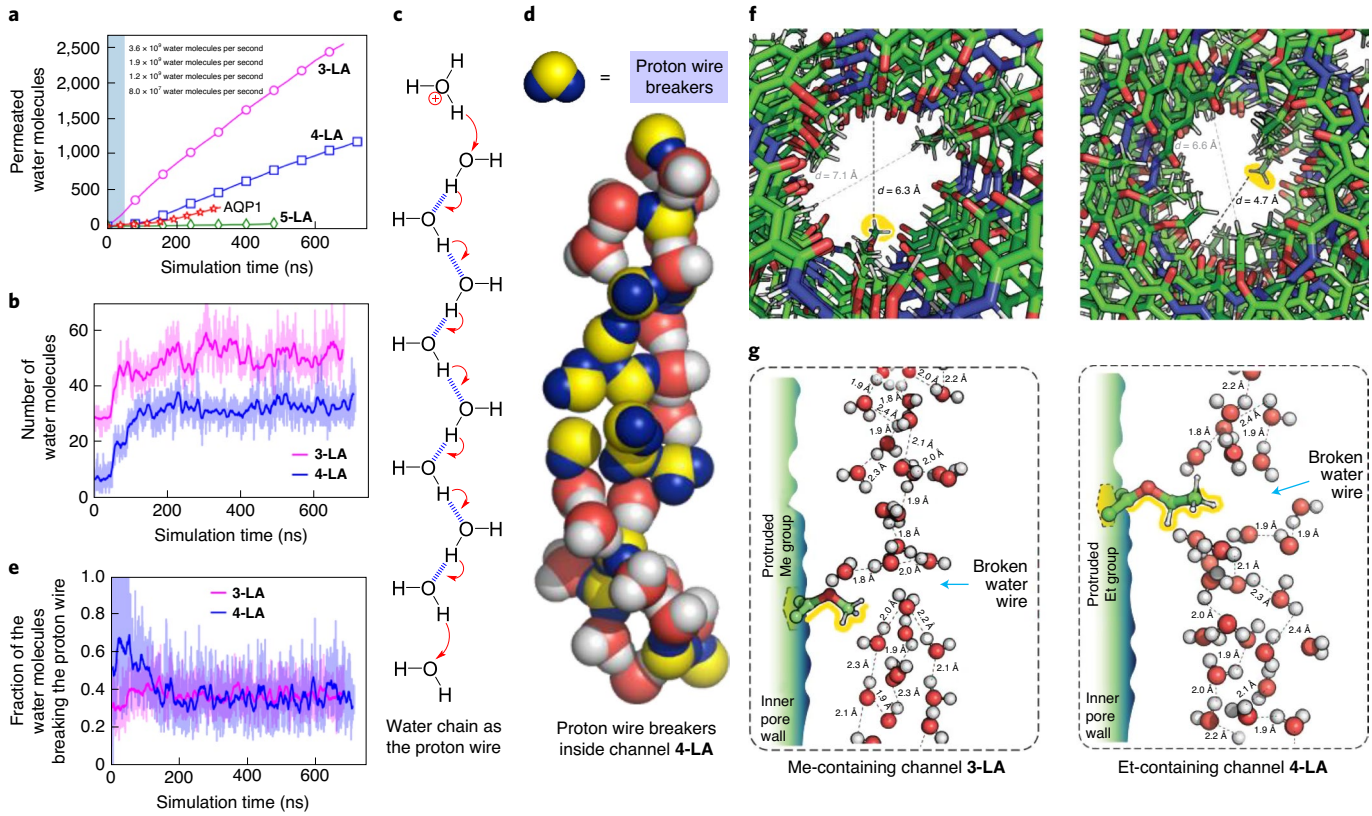

Fig. 3 | MD simulations of water transport and mechanism of proton rejection by proton wire breakers created due to presence of fluctuating alkyl groups. a, Number of water molecules observed to pass through **LA**-containing **3**–**5** and AQP1 in equilibrium MD simulations, with the channel structure harmonically restrained for the first 50 ns. The values in the inset indicate the simulated water permeation rates (top to bottom) of the **3-LA**, **4-LA**, AQP1 and **5-LA** channels. **b**, Number of water molecules inside the pores of channels **3-LA** and **4-LA**. **c**, Illustration of proton transport through an ideal proton wire via the Grotthuss mechanism. **d**, Irregularly H-bonded water molecules, serving as proton wire breakers to block proton transport via the Grotthuss mechanism. **e**, Fractions of proton wire breakers over all the water molecules inside **3-LA** and **4-LA**. **f**, Inward protrusions of Me and Et groups transiently reduce the local cross-section of channels **3-LA** and **4-LA**. *d*, local pore size. **g**, Breakage of proton water wire caused by protrusion of Me (left) and Et (right) groups.

of **3-LA** was measured, and its water-to-salt permselectivity was compared with the values of the other representative membrane materials[10,12,13,34]. Cl^- ion permeability was measured using stopped-flow fluorescence analysis, with lucigenin dyes as molecular sensing probes (Fig. 2f), as demonstrated in a recent study[31]. We chose to use Cl^- transport to provide a conservative value because fluorescent dyes sensitive to Cl^- were found to be more sensitive sensors in a recent study[31].

Quantitative Cl^- permeation through a DOPC membrane in the absence and presence of **3-LA** was measured at several different inwardly directed concentration gradients (Fig. 2g and Supplementary Fig. 13a). Based on the channel density in the membrane, the single-channel Cl^- ion permeability was calculated to be $9.5 \pm 7.5 \times 10^{-21}$ cm^3 s^{-1} for **3-LA**. As shown in Fig. 2h, the water-to-salt permselectivity of **3-LA** was calculated as $1.6 \pm 2.5 \times 10^8$, which overcomes the permeability–selectivity trade-off trendline of currently available desalination membranes[10,12] by a factor of ~10^3, demonstrating good potential for using foldamer-derived AWCs in desalination membrane development.

MD simulation of water transport and proton rejection mechanism

Equilibrium MD simulations of **LA**-containing **3**–**5** (2.9 nm long, each having 26 units of **1** and 25 units of **2**) and of AQP1 embedded in a solvated POPC membrane (Fig. 1c and Supplementary Fig. 14) yielded water permeation rates of 3.60, 1.90, 1.20 and 0.08×10^9 water molecules per second for **3-LA**, **4-LA**, AQP1 and **5-LA**, respectively (Fig. 3a and Supplementary Videos 1–3). Although these values do not exactly match the experimental values, they do show a comparable trend, that is, both **3-LA** and **4-LA** are more permeable to water than AQP1, with **5-LA** being the least permeable. After their non-hydrogen atoms were no longer restrained to the coordinates of the initial ideal model, **3-LA** and **4-LA** were observed to accommodate considerably more water molecules (Fig. 3b), giving rise to considerable increases in water flux. Interestingly, the **LA** groups were observed to flop around the channel's termini, occasionally stacking at the rim of the channel (Supplementary Videos 1–3). While a small defect is evident in the structure of **3-LA** and some water molecules transiently attach to the channel's outer surface, we do not see any transmembrane water permeation through the defects or along the outer surface. The fact that experimental water transport rates between structurally similar **4** and **4-LA** differ by more than sixfold clearly suggests that water moving around the channel to pass through the membrane is not primarily responsible for the high water transport rate seen in **4-LA**. Thus, water transport outside the central channels is likely negligible. Meanwhile, we found **5-LA** to barely contain or conduct any water. This qualitative disagreement with the experimental data is attributable to the initial structural model of the channel, which may not truly represent the relaxed configuration

in the membrane and the simulation time scale, which was too short for the channel to achieve its equilibrium configuration.

At first sight, the many water molecules within these channels (~48 inside **3-LA** and ~33 inside **4-LA**; Fig. 3b) should readily facilitate proton transport, which nevertheless is not observed experimentally. According to the Grotthuss mechanism, a water chain forms a proton wire for proton transport when every water molecule of the chain forms two H bonds with its neighbours, one using its O atom and another one using its H atom (Fig. 3c). Conversely, water molecules forming no bond or just one H bond, or forming two H bonds both solely via only O or only H atoms, can be described as proton wire breakers, blocking proton transport through a water chain (Fig. 3d). The latter is observed in AQPs, where water molecule(s) in the approximate centre of the channel form up to two H bonds with the adjacent water molecules using only H atoms, because the O atoms of these central water molecules are H-bonded by the asparagine–proline–alanine motif[50]. Thus, a proton is not able to hop on or off these water molecules. Nevertheless, as suggested by few, we acknowledge that the electrostatic effect of positively charged residues lining the pore may play an important—perhaps even a predominant role—in inhibiting proton passage through AQPs[45]. In this work, we find that the molecular architecture of **3-LA** and **4-LA** creates several such proton wire breakers that prevent proton hopping through the water molecules, and that these proton wire breakers alone seem to be sufficient to achieve a high level of proton rejection. On average, about 36% water molecules in **3-LA** and **4-LA** are found to satisfy the criteria of being proton wire breakers (Fig. 3e). One statistically meaningful snapshot in Fig. 3d illustrates 15 proton wire breakers and 20 regularly H-bonded water molecules in **4-LA**. Supplementary Fig. 17 highlights a snapshot of **3-LA**, having 26 proton wire breakers and 27 regularly H-bonded water molecules. The presence of these proton wire breakers reduces the average length of a single-file H-bonded water chain from 29.0 Å to 12.5 ± 1.5 Å for **3-LA** and 10.6 ± 0.4 Å for **4-LA**.

To gain further insights into the proton rejection mechanism in **3-LA** and **4-LA**, we investigated the spatio-temporal dynamics of the intra-water H-bonded networks. For our analysis, we split the channel's volume into seven disk-like zones. The MD trajectories of the channels were analysed to quantify the number of breaks in the water chain and the effective pore size in each of the zones using PoreAnalyzer module of PoreDesigner software[53]. Out of 500 MD frames (Supplementary Fig. 18), 67% and 79% have at least one break in the water wire network for **3-LA** (an average of 1.65 breaks per channel) and **4-LA** (an average of 1.86 breaks per channel), respectively. These indicate that for more than two-thirds of the simulation time, there exists no route for protons to permeate through these channels by hopping from one H-bonded water molecule to another via short-lived hydronium ion formation. For the remaining one-third of the MD frames, it is possible that they may be undergoing transitions from one broken proton wire conformation to another, assuming that these transitions may occur at a rate slower than the rate at which the MD frames were collected. The inward-facing Me and Et groups of the Me-containing **3-LA** and Et-containing **4-LA** were found to protrude by up to 1.84 Å and 2.75 Å, respectively, from the pore wall into the water-filled pore (Fig. 3f). These protrusions not only cause fluctuation in the local pore size from 5.2 Å to 7.1 Å for **3-LA** and from 4.6 Å to 6.7 Å for **4-LA** but also a break in the water chain (Fig. 3g). For **3-LA**, 86% disks with an average Me-group protrusion length of 1.74 Å show a break in the water chain. In **4-LA**, 91% disks with an average Et-group protrusion length of 2.64 Å are associated with a break (Supplementary Fig. 18). This proton-blocking mechanism in which the proton wire breaks occur at various locations along the channel by fluctuating hydrophobic interior groups is unprecedented, and it synergistically works with the many proton wire breakers to endow channels **3-LA** and **4-LA** with a high degree of proton exclusion.

Table 1 | Computed number of intermolecular H bonds per water molecule formed among water molecules in the channel, and between water molecule and channel's inner wall[a]

	3-LA	4-LA	AQP1
Water–water	2.0 (±0.2)	1.9 (±0.3)	1.6 (±0.1)
Water–wall	0.8 (±0.1)	0.8 (±0.1)	1.6 (±0.1)
Total	2.8 (±0.3)	2.7 (±0.4)	3.2 (±0.2)

[a]Average values and standard deviations in H bonds were computed for the whole simulation trajectory after excluding the first 50 ns of the simulation where the channels were harmonically restrained (Supplementary Fig. 19a–c).

Lastly, to estimate the E_a value for water entry into the channels, we computed the number of H bonds per water molecule formed between water and the channel wall, as well as among the water molecules for all three channels (Table 1 and Supplementary Fig. 19a–c). Taking 5.1 kcal mol^{-1} as the H-bond energy obtained from an isolated water dimer and each water forming four H bonds in bulk water[54,55], the activation energies can be estimated to be 6.1, 6.3 and 4.1 kcal mol^{-1} for **3-LA**, **4-LA** and AQP1, respectively. These values are consistent with their respective experimental activation energies of 8.7, 8.3 and 5.0 kcal mol^{-1}. We have further used the replica-exchange umbrella sampling method to compute the free energy profile of water molecules translocating through **3-LA**, **4-LA** and AQP1 channels embedded in a POPC lipid bilayer membrane (Supplementary Fig. 19d). Consistent with the experimentally determined activation energies, both **3-LA** and **4-LA** are found to have a higher barrier (~3 kcal mol^{-1}) than AQP1 (~1 kcal mol^{-1}) for water to translocate throughout the pore as seen from the potential of mean force (PMF) calculations. Although the barrier and activation energies for water permeation are both higher in **3-LA** and **4-LA** than in AQP1, we observe more water permeation in these two AWCs than AQP1 in equilibrium simulations. As discussed earlier, this could be due to the wider pores of AWCs as well as the lower number of H bonds formed between water molecules and the pore-lining functional groups (0.8 H bonds per water molecule for AWCs versus 1.6 H bonds per water molecule for AQP1; Table 1), making water movement in AWCs more frictionless.

Summary

In summary, we have presented here novel strategies for the molecular evolution of foldamer-based ultrapermeable AWCs, derived from a fully H-bonded, helically folded pore-forming hydrazide backbone. Tuning of interior groups and attachment of LAs were exploited to enhance the water permeability and salt rejection. Exhibiting ultrahigh single-channel water permeability of 2.7×10^{10} water molecules per second, the most permeable channel **4-LA** further possesses high capacity to reject both salts and protons. This is the first nanometre-sized AWC truly emulating the key water transport features of biological water channels. This ultrapermeable artificial AQP might have the potential to become the preferred candidate for fabricating next-generation membranes for water purification as well as other challenging nanobiotechnological applications where high water transport in addition to proton and ion exclusion are required. Going beyond the specific designs presented here, we can envision a variety of foldamer-based hydrazide water channels, made up of different types of helicity codon[32], having similar intermediate pore sizes as **4-LA**, paralleling or even surpassing the water transport performances of **4-LA**.

Online content

Any methods, additional references, Nature Research reporting summaries, source data, extended data, supplementary

information, acknowledgements, peer review information; details of author contributions and competing interests; and statements of data and code availability are available at https://doi.org/10.1038/s41565-021-00915-2.

Received: 12 June 2020; Accepted: 6 April 2021;
Published online: 20 May 2021

References

1. Murata, K. et al. Structural determinants of water permeation through aquaporin-1. *Nature* **407**, 599–605 (2000).
2. Tajkhorshid, E. et al. Control of the selectivity of the aquaporin water channel family by global orientational tuning. *Science* **296**, 525–530 (2002).
3. Takata, K., Matsuzaki, T. & Tajika, Y. Aquaporins: water channel proteins of the cell membrane. *Prog. Histochem. Cytochem.* **39**, 1–83 (2004).
4. de Groot, B. L. & Grubmuller, H. Water permeation across biological membranes: mechanism and dynamics of aquaporin-1 and GlpF. *Science* **294**, 2353–2357 (2001).
5. Agre, P. Aquaporin water channels (Nobel lecture). *Angew. Chem. Int. Ed.* **43**, 4278–4290 (2004).
6. Borgnia, M. J., Kozono, D., Calamita, G., Maloney, P. C. & Agre, P. Functional reconstitution and characterization of AqpZ, the *E. coli* water channel protein. *J. Mol. Biol.* **291**, 1169–1179 (1999).
7. Horner, A. et al. The mobility of single-file water molecules is governed by the number of H-bonds they may form with channel-lining residues. *Sci. Adv.* **1**, e1400083 (2015).
8. Fane, A. G., Wang, R. & Hu, M. X. Synthetic membranes for water purification: status and future. *Angew. Chem. Int. Ed.* **54**, 3368–3386 (2015).
9. Werber, J. R., Osuji, C. O. & Elimelech, M. Materials for next-generation desalination and water purification membranes. *Nat. Rev. Mater.* **1**, 16018 (2016). https://doi.org/10.1038/natrevmats.2016.18
10. Park, H. B., Kamcev, J., Robeson, L. M., Elimelech, M. & Freeman, B. D. Maximizing the right stuff: the trade-off between membrane permeability and selectivity. *Science* **356**, eaab0530 (2017).
11. Hélix-Nielsen, C. Biomimetic membranes as a technology platform: challenges and opportunities. *Membranes* **8**, 44–59 (2018).
12. Werber, J. R. & Elimelech, M. Permselectivity limits of biomimetic desalination membranes. *Sci. Adv.* **4**, eaar8266 (2018).
13. Freger, V. Selectivity and polarization in water channel membranes: lessons learned from polymeric membranes and CNTs. *Faraday Discuss.* **209**, 371–388 (2018).
14. Wagh, P. & Escobar, I. C. Biomimetic and bioinspired membranes for water purification: a critical review and future directions. *Environ. Prog. Sustainable Energy* **38**, e13215 (2019).
15. Barboiu, M. & Gilles, A. From natural to bioassisted and biomimetic artificial water channel systems. *Acc. Chem. Res.* **46**, 2814–2823 (2013).
16. Huo, Y. P. & Zeng, H. Q. 'Sticky'-ends-guided creation of functional hollow nanopores for guest encapsulation and water transport. *Acc. Chem. Res.* **49**, 922–930 (2016).
17. Gong, B. Artificial water channels: inspiration, progress, and challenges. *Faraday Discuss.* **209**, 415–427 (2018).
18. Song, W. & Kumar, M. Artificial water channels: toward and beyond desalination. *Curr. Opin. Chem. Eng.* **25**, 9–17 (2019).
19. Bhushan, B. Biomimetics: lessons from nature–an overview. *Phil. Trans. R. Soc. A* **367**, 1445–1486 (2009).
20. Doyle, D. A. et al. The structure of the potassium channel: molecular basis of K^+ conduction and selectivity. *Science* **280**, 69–77 (1998).
21. Yu, F. H. & Catterall, W. A. Overview of the voltage-gated sodium channel family. *Genome Biol.* **4**, 207 (2003).
22. Reuter, H. Membranes: a variety of calcium channels. *Nature* **316**, 391 (1985).
23. Dutzler, R., Campbell, E. B. & MacKinnon, R. Gating the selectivity filter in ClC chloride channels. *Science* **300**, 108–112 (2003).
24. Mould, J. A. et al. Mechanism for proton conduction of the M_2 ion channel of influenza A virus. *J. Biol. Chem.* **275**, 8592–8599 (2000).
25. Kaucher, M. S. et al. Selective transport of water mediated by porous dendritic dipeptides. *J. Am. Chem. Soc.* **129**, 11698–11699 (2007).
26. Zhou, X. B. et al. Self-assembling subnanometer pores with unusual mass-transport properties. *Nat. Commun.* **3**, 949 (2012).
27. Hu, C. B., Chen, Z. X., Tang, G. F., Hou, J. L. & Li, Z. T. Single-molecular artificial transmembrane water channels. *J. Am. Chem. Soc.* **134**, 8384–8387 (2012).
28. Licsandru, E. et al. Salt-excluding artificial water channels exhibiting enhanced dipolar water and proton translocation. *J. Am. Chem. Soc.* **138**, 5403–5409 (2016).
29. Zhao, H. Q., Sheng, S., Hong, Y. H. & Zeng, H. Q. Proton gradient-induced water transport mediated by water wires inside narrow aquapores of aquafoldamer molecules. *J. Am. Chem. Soc.* **136**, 14270–14276 (2014).
30. Shen, Y.-X. et al. Highly permeable artificial water channels that can self-assemble into two-dimensional arrays. *Proc. Natl Acad. Sci. USA* **112**, 9810–9815 (2015).
31. Song, W. et al. Artificial water channels enable fast and selective water permeation through water-wire networks. *Nat. Nanotechnol.* **15**, 73–79 (2020).
32. Shen, J. et al. Polypyridine-based helical amide foldamer channels: rapid transport of water and protons with high ion rejection. *Angew. Chem. Int. Ed.* **59**, 13328–13334 (2020).
33. Shen, J. et al. Aquafoldmer-based aquaporin-like synthetic water channel. *J. Am. Chem. Soc.* **142**, 10050–10058 (2020).
34. Tunuguntla, R. H. et al. Enhanced water permeability and tunable ion selectivity in subnanometer carbon nanotube porins. *Science* **357**, 792–796 (2017).
35. Gale, P. A., Davis, J. T. & Quesada, R. Anion transport and supramolecular medicinal chemistry. *Chem. Soc. Rev.* **46**, 2497–2519 (2017).
36. Sakai, N. & Matile, S. Synthetic ion channels. *Langmuir* **29**, 9031–9040 (2013).
37. Si, W., Xin, P., Li, Z.-T. & Hou, J.-L. Tubular unimolecular transmembrane channels: construction strategy and transport activities. *Acc. Chem. Res.* **48**, 1612–1619 (2015).
38. Howorka, S. Building membrane nanopores. *Nat. Nanotechnol.* **12**, 619–630 (2017).
39. Zheng, S.-P., Huang, L.-B., Sun, Z. & Barboiu, M. Self-assembled artificial ion-channels toward natural selection of functions. *Angew. Chem. Int. Ed.* **60**, https://doi.org/10.1002/anie.201915287 566–597 (2020).
40. Roy, A. et al. Polyhydrazide-based organic nanotubes as efficient and selective artificial iodide channels. *Angew. Chem. Int. Ed.* **59**, 4806–4813 (2020).
41. Tunuguntla, R. H., Allen, F. I., Kim, K., Belliveau, A. & Noy, A. Ultrafast proton transport in sub-1-nm diameter carbon nanotube porins. *Nat. Nanotechnol.* **11**, 639–644 (2016).
42. Ren, C. et al. Molecular swings as highly active ion transporters. *Angew. Chem. Int. Ed.* **58**, 8034–8038 (2019).
43. Zeng, L. Z., Zhang, H., Wang, T. & Li, T. Enhancing K^+ transport activity and selectivity of synthetic K^+ channels via electron-donating effects. *Chem. Commun.* **56**, 1211–1214 (2020).
44. Chen, F. et al. Pyridine/oxadiazole-based helical foldamer ion channels with exceptionally high K^+/Na^+ selectivity. *Angew. Chem. Int. Ed.* **59**, 1440–1444 (2020).
45. de Groot, B., Frigato, T., Helms, V. & Grubmüller, H. The mechanism of proton exclusion in the aquaporin-1 water channel. *J. Mol. Biol.* **333**, 279–293 (2003).
46. Pohl, P., Saparov, S. M., Borgnia, M. J. & Agre, P. Highly selective water channel activity measured by voltage clamp: analysis of planar lipid bilayers reconstituted with purified AqpZ. *Proc. Natl Acad. Sci. USA* **98**, 9624–9629 (2001).
47. Pham, T. A. et al. Salt solutions in carbon nanotubes: the role of cation–π interactions. *J. Phys. Chem. C* **120**, 7332–7338 (2016).
48. Kim, K. et al. Crystal structure and functional characterization of a light-driven chloride pump having an NTQ motif. *Nat. Commun.* **7**, 12677 (2016).
49. Ren, C. L. et al. Pore-forming monopeptides as exceptionally active anion channels. *J. Am. Chem. Soc.* **140**, 8817–8826 (2018).
50. Kosinska Eriksson, U. et al. Subangstrom resolution X-ray structure details aquaporin-water interactions. *Science* **340**, 1346–1349 (2013).
51. Horner, A., Siligan, C., Cornean, A. & Pohl, P. Positively charged residues at the channel mouth boost single-file water flow. *Faraday Discuss.* **209**, 55–65 (2018).
52. Ren, C. et al. A halogen bond-mediated highly active artificial chloride channel with high anticancer activity. *Chem. Sci.* **9**, 4044–4051 (2018).
53. Chowdhury, R. et al. PoreDesigner for tuning solute selectivity in a robust and highly permeable outer membrane pore. *Nat. Commun.* **9**, 3661 (2018).
54. Zhang, C., Wu, J., Galli, G. & Gygi, F. Structural and vibrational properties of liquid water from van der Waals density functionals. *J. Chem. Theory Comput.* **7**, 3054–3061 (2011).
55. Li, Y. et al. Water-ion permselectivity of narrow-diameter carbon nanotubes. *Sci. Adv.* **6**, eaba9966 (2020).

Methods

Typical polymerization conditions. In a 20 ml reaction vial, 2-alkoxyisophthalic acid (**1a**–**1b**; 0.118 mmol) and 4,6-bis(octyloxy)isophthalohydrazide (**2**; 0.118 mmol) were introduced. Coupling reagents (0.354 mmol) were added to each reaction vial. This was followed by adding freshly distilled CH_2Cl_2 (5 ml) and 1 ml dimethylformamide (DMF) in a N_2 atmosphere. Then, 100 µl *N*,*N*-diisopropyl ethylamine was added in the reaction mixture, and the solution was stirred for 2 days at room temperature. After completion of reaction, the solvent was evaporated to remove CH_2Cl_2 and DMF. The obtained residue was first washed with 10 ml MeOH/H_2O (1:1) and subsequently washed with 10 ml water and 10 ml MeOH and dried in an oven (60 °C) to obtain polymers **3**–**5** as an off-white solid powder with yields of 60–80%. Average molecular weights (M_n) of all these polymers were determined by gel permeation chromatography.

Water transport and salt rejection study using a stopped-flow instrument. DOPC (0.24 ml and 25 mg ml^{-1} in $CHCl_3$; Avanti Polar Lipids) and channel samples (**3**–**5** with and without LA or gA in $CHCl_3$) were mixed at different mLCR values (1,500:1 to 9,000:1) in micro-tubes (2 ml). The solvent was removed by a N_2 flow and the resulting film was dried under a high vacuum overnight. HEPES buffer (10 mM HEPES and 100 mM NaCl; pH 7, 1.0 ml) was then added, followed by vortexing the solution for 30 s and then ten cycles of sonication (37 kHz, 100% power, 70 °C, 2.5 min) to maximize the incorporation extent of channel molecules into the membrane. A glass spatula was used if necessary to make sure the residue was fully detached from the surface of the micro-tube. The mixture was further subjected to ten freeze–thaw cycles (freezing in liquid N_2 for 1 min and heating at 55 °C in a water bath for 2 min) and extruded at 80 °C for 15 times. The LUVs obtained in this way contained 6 mg ml^{-1} lipids and were stored in a 4 °C fridge before use, and diluted six times with HEPES buffer to make 1 mg ml^{-1} LUV for the stopped-flow measurements. The particle size of LUV (120 nm) was characterized by dynamic light scattering (Zetasizer Nano, Malvern Instruments). The water permeability measurements were conducted on a stopped-flow instrument (Chirascan circular dichroism spectrometer, Applied Photophysics). Exposure of vesicles to three types of hypertonic osmolytes resulted in the shrinkage of the vesicles due to an outwardly directed osmotic gradient. The abrupt decrease in the vesicle size leads to an increase in the light scattering intensity at 90° according to the Rayleigh–Gans theory. The changes in light scattering intensity caused by vesicle shrinkage were recorded at a wavelength of 577 nm, and were fitted in the following form of a single exponential function.

$$y = A \times \exp(-kx) + y_0$$

where y is the change in light scattering, k is the exponential coefficient of the change in light scattering, x is the time, and A and y_0 are the two constants.

With the assumption that the change in light scattering intensity is proportional to change in the vesicle volume ($\Delta V/V_0$) based on the Boyle–van't Hoff law, P_f in the unit of cm s^{-1} was calculated as follows:

$$P_f = k/((S/V_0) \times V_w \times \Delta_{osm})$$

where k is the exponential coefficient of the change in the light scattering; S and V_0 are the initial surface area and initial volume of the vesicles, respectively; V_w is the molar volume of water; and Δ_{osm} is the osmolarity difference.

To calculate the true water permeability (P_{sc} in the unit of cm^3 s^{-1}) of water channels, the $P_{f(blank)}$ value of the blank vesicle without water channels needs to be deducted from the $P_{f(channel)}$ value of the vesicle with water channels, which was multiplied by the vesical surface area (S) and divided by the number of water channels (N) incorporated in the liposome as shown below.

$$P_{sc} = \left(P_{f(channel)} - P_{f(blank)}\right) \times (S/N)$$

The ability of **4-LA** to reject salts was first evaluated by comparing the osmotic water permeability (P_f in cm s^{-1}) values under three hypertonic buffer solutions (300 mM sucrose, 150 mM NaCl or 150 mM KCl; Supplementary Fig. 6).

Determination of channel insertion efficiency. To calculate the channel insertion efficiency of water channels in the lipid bilayer membrane, a calibration curve was first created. At first, blank LUVs (without any synthetic channels) were prepared with concentration ranging from 3 to 7 mg ml^{-1} by using the film rehydration method (without extrusion) as discussed above. All these solutions were scanned on an ultraviolet–visible (UV–vis) spectrometer; the ultraviolet (UV) absorbance was found to decrease proportionally with a decrease in concentration. Calibration curve was plotted using these UV–vis data at 280 nm. Blank LUVs were also prepared by extruding through a 200 nm membrane for 15 times to obtain monodispersed unilamellar vesicles with an initial concentration of 6 mg ml^{-1}, which is equivalent to our experimental condition. UV absorbance was recorded with these extruded blank liposomes at 280 nm wavelength. The obtained data were used to get the actual lipid concentration, that is, 4.4 ± 0.7 mg ml^{-1}, and around 20% lipid was lost during the extrusion process.

Since the concentration of synthetic water channels is extremely low compared with lipid concentration in our experimental condition, the UV absorbance plots of the lipid were found to be superimposed with the absorbance values of channels. Therefore, we measured the fluorescence spectra of channel-containing liposomes ($\lambda_{excitation}$ = 310 nm and $\lambda_{emission}$ = 430 nm for the channel molecules). In these experiments, two separate batches of liposomes, embedded with AWCs, were prepared using the film rehydration method as discussed earlier for each concentration ratio. One of the batches was not extruded and the other batch was extruded through a 200 nm membrane for 15 times to obtain monodispersed LUVs. Fluorescence spectra were recorded for all these channel-containing liposomes. Considering the lipid loss from the UV–vis experiment and the ratio between the fluorescence intensities (at $\lambda_{emission}$ = 430 nm) of non-extruded and extruded liposomes provided us the value of insertion efficiency of AWCs in the lipid membrane. The obtained insertion efficiency values were further used to calculate the actual single-channel water permeability of AWCs.

Activation energy measurements. To determine the activation energies for water transport, water transport kinetics was measured by using a stopped-flow instrument from 6 to 25 °C. For these experiments, the temperatures of the solution reservoir and measurement cell of the stopped-flow instrument were maintained by a recirculating heater/chiller (Polystat, Cole-Parmer). Light-scattering kinetic rates representing water transport through the AWCs at varying temperatures were fitted into the following Arrhenius equation to obtain the activation energy.

$$\ln(k) = \ln(A) - E_a/(R \times T)$$

where k is the exponential coefficient of the change in light scattering, A is a pre-exponential factor, E_a is the activation energy, R is a gas constant and T is the absolute temperature.

Cl^- ion permeability measurement. Cl^- ion permeability was measured using stopped-flow fluorescence analysis, with lucigenin dyes as the molecular sensing probes. The transport rate obtained from these analyses was used to represent the net monovalent ion (for example, Na^+ and Cl^-) permeability of the channels. This method gives a conservative estimate of the monovalent ion permeability because in actual desalination processes, Cl^- permeation is up to three orders of magnitude lower, as it is limited by the lower Na^+ ion permeability and the condition of electroneutrality. Therefore, many analytical studies have adopted Na^+ ions as a model molecule to analyse desalination processes. DOPC and **3-LA**-reconstituted DOPC liposomes were prepared using the same method of preparing the samples for water permeability measurements, except that a different rehydration buffer composition was used (1 mM lucigenin, 10 mM HEPES, 200 mM KNO_3 and 10 µM valinomycin at pH 7). The K^+ ionophore valinomycin was added to mitigate the electrostatic imbalance caused by Cl^- permeation. After extrusion, the reconstituted vesicles were purified by Sephadex G-50 columns to remove free (unencapsulated) lucigenin dyes. The vesicles were exposed to the Cl^--containing buffer in the stopped-flow equipment, and quantitative Cl^- flux was calculated by the Stern–Volmer equation as follows.

$$\frac{F}{F_0} - 1 = K_{sv}\left[Cl^-\right]$$

where F is the fluorescence intensity change inside the vesicles over time; F_0 is the initial fluorescence intensity at the Cl^--free condition, which corresponds to the initial (time t = 0) fluorescence intensity from the stopped-flow experiments; $[Cl^-]$ is the molar concentration of chloride inside the vesicles; and K_{sv} is the Stern–Volmer constant of the dye. The K_{sv} of the dye sensor within DOPC vesicles was experimentally determined, as shown in Supplementary Fig. 13b. Permeability calculation was performed by utilizing the first derivative of the Stern–Volmer equation with respect to time (at time approaching zero) as shown below.

$$\left.\frac{d\left[Cl^-\right]}{dt}\right|_{t=0} = \frac{-1}{K_{sv}F_0}\left.\frac{dF}{dt}\right|_{t=0}$$

From the left-hand side of this equation, quantitative Cl^- concentration change was calculated and influx of Cl^- through the vesicular membranes was calculated based on the size of the vesicles. The measurements were repeated at different concentration gradients and the permeability coefficients were calculated from these datasets.

Fluorescence correlation spectroscopy to determine channel density of 3-LA in lipid membranes for the calculation of single-channel Cl^- permeability. 3-LA channels were labelled with 5-(and-6-)-((*N*-(5-aminopentyl)amino) carbonyl) tetramethylrhodamine fluorescence dyes using dicyclohexyl carbodiimide crosslinkers by mixing the channels, dyes and crosslinkers at a molar ratio of 1:10:10 in dimethylsulfoxide for 24 h at room temperature using a previously used procedure. Unreacted free dyes were removed by dialysis with fresh dimethylsulfoxide. These dye-labelled channels were then used to prepare the **3-LA**-reconstituted DOPC vesicles, and these vesicles were subjected to fluorescence correlation spectroscopy experiments. The time-dependent fluorescence fluctuation inside the confocal volume was monitored using a Zeiss

confocal laser scanning microscope (LSM 880) equipped with the Airyscan detector. A diode-pumped solid state laser with an excitation wavelength of 561 nm at 20 mW was used to measure the emission intensity in the wavelength range from 570 to 695 nm. The average number of vesicles and micelles was measured for 10 s, obtaining 10 counts and through 3 repeated fluorescence correlation spectroscopy measurements. The collected autocorrelation curves, $G(\tau)$, were fitted with the triplet state and translation parameters using the ZEN software (black edition).

$$G(\tau) = \frac{1}{N}\sum_{i=0}^{M} f_i \left[\frac{1}{1+\tau/\tau_{D_i}}\right]\left[\frac{1}{1+(r/z)^2(\tau/\tau_{D_i})}\right]^{1/2}$$

where τ is the lag time; r and z are the radius and half height of the confocal space, respectively; τ_{D_i} is the lateral diffusion time of fluorescence species i; and N is the average number of fluorescence species in the confocal space. From this function, the number of **3-LA**-reconstituted vesicles were extracted (N_{ves}). After that, the same vesicle samples were completely micellized by adding a final concentration of 4% (w/v) octyl β-d-glucoside and the sample analysis was repeated to obtain the average number of micellized channels ($N_{channel}$). From the ratio of $N_{channel}$ to N_{ves}, the channel number density in the DOPC vesicular membranes was determined (Supplementary Fig. 13c).

HPTS assay for cation transport study under high salt gradient. Thirty microlitres of HPTS-containing LUVs (Supplementary Information provides the detailed protocol) were added to 1,970 µl HEPES buffer (10 mM HEPES and 200 mM M_2SO_4 ($M^+ = Na^+$ and K^+) at pH 8) in a clean fluorescence cuvette to generate a salt gradient across the lipid bilayer. This cuvette was placed on the fluorescence instrument (at $t = 0$ s) equipped with a magnetic stirrer. Fluorescence emission intensity of HPTS dye, F_t, was monitored at $\lambda_{em} = 510$ nm ($\lambda_{ex} = 450$ nm) with time. Channels of various types (1 µM, dissolved in DMF) were added at $t = 70$ s and simultaneously recorded for 300 s using a fluorescence spectrophotometer (Hitachi, model F-7100). Finally, at $t = 370$ s, 20 µl of 20% Triton-X100 was added to destroy all vesicles, which resulted in destruction of the pH gradient to achieve the maximum change in fluorescence emission intensity of the HPTS dye. Fluorescence data were also recorded for gA (2 µM) under the same experimental condition, and the obtained activity was compared with AWCs.

The time axis was offset according to the following equation: $t = t - 70$. Fluorescence intensities (F_t) were normalized to the fractional emission intensity I_F using the following equation:

$$I_F = [(F_t - F_0)/(F_\infty - F_0)] \times 100$$

where F_0 is the fluorescence intensity just before the compound addition (at $t = 0$ s), F_∞ is the fluorescence intensity at saturation after complete leakage (at $t = 300$ s) and F_t is the fluorescence intensity at time t.

HPTS assay for anion and proton transport study. Thirty microlitres of HPTS-containing LUVs (Supplementary Information provides the detailed protocol) were added to 1,970 µl HEPES buffer (10 mM HEPES, 67 mM K_2SO_4, pH 8) in a clean fluorescence cuvette to generate a salt gradient across the lipid bilayer. This cuvette was placed on the fluorescence instrument (at $t = 0$ s) equipped with a magnetic stirrer. Fluorescence emission intensity of HPTS dye, F_t, was monitored at $\lambda_{em} = 510$ nm ($\lambda_{ex} = 450$ nm) with time. Channels (**3**, **4**, **5** and **L8**) or proton carrier (FCCP) at the desired concentration in DMF was added at $t = 70$ s and simultaneously recorded for 300 s using a fluorescence spectrophotometer (Hitachi, model F-7100). Finally, at $t = 370$ s, 20 µl of 20% Triton-X100 was added to destroy all vesicles, which resulted in destruction of the pH gradient to achieve the maximum change in fluorescence emission intensity of the HPTS dye. Exchange via H^+/M^+ antiport mechanism was monitored by change in fluorescence intensity of the HPTS dyes in the presence of a high salt gradient (200 mM Na_2SO_4 or K_2SO_4).

The time axis was offset according to the following equation: $t = t - 70$. Fluorescence intensities (F_t) were normalized to the fractional emission intensity I_F using the following equation:

$$I_F = [(F_t - F_0)/(F_\infty - F_0)] \times 100$$

where F_0 is the fluorescence intensity just before the compound addition (at $t = 0$ s), F_∞ is the fluorescence intensity at saturation after complete leakage (at $t = 300$ s) and F_t is the fluorescence intensity at time t.

SPQ assay for anion transport activity study. The SPQ-containing LUV suspension (30 µl, 10 mM in 225 mM $NaNO_3$) was added to an NaCl solution (1.7 ml, 225 mM) to create an extravesicular chloride gradient. A solution of channel molecule **3-LA**, **4-LA** and **5-LA** (1 µM) or anion channel **L8** (6 µM) in DMF at different concentrations was then injected into the suspension under gentle stirring. Upon the addition of channels, the emission of SPQ was immediately monitored at 430 nm with excitations at 360 nm for 300 s using a fluorescence spectrophotometer (Hitachi, model F-7100) after which time an aqueous solution of Triton-X100 (20 µl, 20% v/v) was immediately added to completely destroy the chloride gradient. The final transport trace was obtained by normalizing the fluorescence intensity using the following equation:

$$I_F = [(F_t - F_0)/(F_\infty - F_0)]$$

where F_0 is the fluorescence intensity just before the compound addition (at $t = 0$ s), F_∞ is the fluorescence intensity at saturation after complete leakage (at $t = 300$ s) and F_t is the fluorescence intensity at time t.

MD simulations. All MD simulations were performed using the NAMD programme[56] and the periodic boundary conditions. The particle mesh Ewald method was used to calculate the long-range electrostatics[57]. The Nosé–Hoover Langevin piston[58,59] and Langevin thermostat[60] were used to maintain constant pressure and temperature in the system, respectively. CHARMM36 force field parameters[61] described the bonded and non-bonded interactions among the lipid bilayer membranes, water and ions. An 8–10–12 Å cutoff scheme was used to calculate the van der Waals and short-range electrostatic forces. All simulations were performed using a 2 fs time step to integrate the equation of motion. The SETTLE algorithm[62] was applied to keep the water molecules rigid, whereas the RATTLE algorithm[63] constrained all other covalent bonds involving hydrogen atoms. The coordinates of the system were saved at an interval of 19.2 ps. Analysis and post-processing of the simulation trajectories were performed using VMD[64] and CPPTRAJ[65].

To build the initial PDB structures of **LA**-modified channels **3**–**5** with height of 2.9 nm, each having 26 repeating units of **1** and 25 repeating units of **2**, QM at the level of ωB97X/6-31 + G(d) was used to optimize symmetric short pore scaffolds consisting of four repeating units of **1** and five repeating units of **2** (Fig. 1b) that were created using GaussView[66]. Based on these QM-derived structures, which look nearly identical to their corresponding crystal structures shown in Supplementary Fig. 1b in terms of bond angle and cavity enclosed, longer channels, that is, **LA**-modified channels **3**–**5**, were built using GaussView and then subjected to MD simulation. The topology and force field parameters for the monomeric unit of the channel (along with all three variants **3**, **4** and **5**) and the LAs were obtained using the CHARMM general force fields web server[67]. We connected the LAs to the terminal residues and obtained the protein structure file of the channels using the psfgen tool of VMD. The channels were then embedded into a 9×9 nm^2 patch of pre-equilibrated POPC lipid bilayer membrane. The lipid patch was generated using the CHARMM-GUI membrane builder[68] and pre-equilibrated for approximately 400 ns. Lipid molecules that overlapped with the channel were removed. The system was then solvated with water[69] using the solvate plugin of VMD. Sodium and chloride ions were added to 1 M concentration using the autoionize plugin of VMD. The final assembled system measured $9 \times 9 \times 9$ nm^3 and contained approximately 80,000 atoms.

Following the assembly, the system underwent 1,200 steps of energy minimization using the conjugate gradient method to remove steric clashes. After energy minimization, the system was subjected to a 50 ns equilibration at a constant number of atoms (N), pressure ($P = 1$ bar) and temperature ($T = 300$ K) (the NPT ensemble) with harmonic restraints applied to all non-hydrogen atoms of channels that surrounded the transmembrane pore. The restraints were applied relative to the initial coordinates of the atoms, and the spring constants were 1 kcal mol^{-1} Å^{-2}. After 50 ns, the harmonic restraints were removed, and the system was equilibrated free of any restraints for ~700 ns.

The initial all-atom model of AQP embedded in a lipid membrane was taken from a previous study[70] and simulated using the protocols described above.

Reporting Summary. Further information on research design is available in the Nature Research Reporting Summary linked to this article.

Data availability

The datasets that support the finding of this study are available in figshare repository with the identifier(s) https://figshare.com/s/0354959049b2c0ed4c61. Source data are provided with this paper.

References

56. Phillips, J. C. et al. Scalable molecular dynamics with NAMD. *J. Comput. Chem.* **26**, 1781–1802 (2005).
57. Darden, T., York, D. & Pedersen, L. Particle mesh Ewald: an *N*·log(*N*) method for Ewald sums in large systems. *J. Chem. Phys.* **98**, 10089–10092 (1993).
58. Feller, S. E., Zhang, Y., Pastor, R. W. & Brooks, B. R. Constant pressure molecular dynamics simulation: the Langevin piston method. *J. Chem. Phys.* **103**, 4613–4621 (1995).
59. Martyna, G. J., Tobias, D. J. & Klein, M. L. Constant pressure molecular dynamics algorithms. *J. Chem. Phys.* **101**, 4177–4189 (1994).
60. Sindhikara, D. J., Kim, S., Voter, A. F. & Roitberg, A. E. Bad seeds sprout perilous dynamics: stochastic thermostat induced trajectory synchronization in biomolecules. *J. Chem. Theory Comput.* **5**, 1624–1631 (2009).
61. Klauda, J. B. et al. Update of the CHARMM all-atom additive force field for lipids: validation on six lipid types. *J. Chem. Phys. B* **114**, 7830–7843 (2010).

62. Miyamoto, S. & Kollman, P. A. Settle: an analytical version of the SHAKE and RATTLE algorithm for rigid water models. *J. Comput. Chem.* **13**, 952–962 (1992).
63. Andersen, H. C. Rattle: A 'velocity' version of the shake algorithm for molecular dynamics calculations. *J. Comp. Phys.* **52**, 24–34 (1983).
64. Humphrey, W., Dalke, A. & Schulten, K. VMD: visual molecular dynamics. *J. Mol. Graph.* **14**, 33–38 (1996).
65. Roe, D. R. & Cheatham, T. E. III PTRAJ and CPPTRAJ: software for processing and analysis of molecular dynamics trajectory data. *J. Chem. Theory Comput.* **9**, 3084–3095 (2013).
66. Frisch, M.J. et al. Gaussian 16 rev. C.01 (Wallingford CT, 2016).
67. Vanommeslaeghe, K. et al. CHARMM general force field: a force field for drug-like molecules compatible with the CHARMM all-atom additive biological force fields. *J. Comput. Chem.* **31**, 671–690 (2010).
68. Jo, S., Kim, T., Iyer, V. G. & Im, W. CHARMM-GUI: a web-based graphical user interface for CHARMM. *J. Comput. Chem.* **29**, 1859–1865 (2008).
69. Jorgensen, W. L., Chandrasekhar, J., Madura, J. D., Impey, R. W. & Klein, M. L. Comparison of simple potential functions for simulating liquid water. *J. Chem. Phys.* **79**, 926–935 (1983).
70. Decker, K. et al. Selective permeability of truncated aquaporin 1 in silico. *ACS Biomater. Sci. Eng.* **3**, 342–348 (2017).

Acknowledgements

This study was supported by the Institute of Advanced Synthesis, Northwestern Polytechnical University, China; NanoBio Lab (Biomedical Research Council, Agency for Science, Technology and Research, Singapore); the Singapore National Research Foundation under its Environment and Water Research Programme and administered by PUB; the National Science Foundation (USA) under grant no. DMR-1827346; and the National Institutes of Health under grant no. P41-GM104601. The work in M.K.'s lab was supported by the US National Science Foundation under grant nos. CBET 1946392 and CBET 1952295. Supercomputer time was provided through the Early Allocation grant on Frontera (FTA-Chemla), XSEDE Allocation grant no. MCA05S028 and the Blue Waters petascale supercomputer system at the University of Illinois at Urbana–Champaign.

Author contributions

A.R. synthesized polymers **3** and **5** and conducted the water/ion transport study. J.S. synthesized polymer **4** and conducted the water/ion transport study. H.J. and A.A. performed the MD study. W.S., Y.-M.T. and M.K. determined water-over-chloride selectivity and proton transport rates. R.C. and M.K. conducted analysis of proton exclusion simulations. R.Y., N.L. and C.R. performed some ion transport studies. H.Z. conceived the project and wrote the manuscript with inputs from A.R. and M.K. All the authors edited the manuscript.

Competing interests

The authors declare no competing interests.

Additional information

Supplementary information The online version contains supplementary material available at https://doi.org/10.1038/s41565-021-00915-2.

Correspondence and requests for materials should be addressed to H.Z.

Peer review information *Nature Nanotechnology* thanks the anonymous reviewers for their contribution to the peer review of this work.

Reprints and permissions information is available at www.nature.com/reprints.